



Published in final edited form as:

Nat Methods. 2020 September ; 17(9): 928–936. doi:10.1038/s41592-020-0913-x.

Rational design and implementation of a chemically inducible hetero-trimerization system

Helen D. Wu^{1,5}, Masaki Kikuchi², Onur Dagliyan³, Adam K. Aragaki^{4,5}, Hideki Nakamura^{5,8}, Nikolay V. Dokholyan^{6,7}, Takashi Umehara^{2,*}, Takanari Inoue^{1,4,5,*}

¹Department of Biomedical Engineering, Johns Hopkins University School of Medicine, Baltimore, MD 21205

²Laboratory for Epigenetics Drug Discovery, RIKEN Center for Biosystems Dynamics Research, Yokohama, Kanagawa 230-0045, Japan

³Department of Neurobiology, Harvard Medical School, Boston, MA 02115

⁴Department of Pharmacology, Johns Hopkins University School of Medicine, Baltimore, MD 21205

⁵Department of Cell Biology, Center for Cell Dynamics, Johns Hopkins University School of Medicine, Baltimore, MD 21205

⁶Departments of Pharmacology and Biochemistry & Molecular Biology, Penn State University College of Medicine, Hershey, Pennsylvania

⁷Departments of Chemistry and Biomedical Engineering, Pennsylvania State University, University Park, Pennsylvania

⁸Present address: Kyoto University Graduate School of Engineering, Department of Synthetic Chemistry and Biological Chemistry, Katsura Int'tech Center, Graduate School of Engineering, Kyoto University, Nishikyo-ku, Kyoto, 615-8530, Japan

Abstract

Chemically inducible dimerization (CID) uses a small molecule to induce binding of two different proteins. CID tools like the FKBP/FRB/rapamycin system have been widely employed to probe molecular events inside and outside cells. While various CID tools are available, chemically inducible trimerization (CIT) does not exist, due to inherent challenges in designing a chemical that simultaneously binds three proteins with high affinity and specificity. Here, we developed CIT by rationally splitting FRB and FKBP. Cellular and structural datasets showed efficient trimerization of split pairs of FRB or FKBP with full length FKBP or FRB, respectively, by

*Correspondence: Takashi Umehara takashi.umehara@riken.jp for Structural Analysis, Takanari Inoue jctinoue@jhmi.edu for General Correspondence.

Author contributions

H.D.W. and H.N. conceived the study with input from T.I. H.D.W. carried out cell experiments and conducted image analysis with help from A.K.A. M.K. purified and crystalized split proteins, and determined protein structure by X-ray crystallography. O.D. conducted rational split site analysis. T.I., H.N., T.U., and N.V.D. supervised the project. H.D.W. wrote the manuscript in consultation with T.I. and with input from M.K., T.U., O.D., and N.V.D.

Competing Interests

There is an ongoing disclosure associated with the CIT tools.

rapamycin. CIT rapidly induced tri-organellar junctions, and perturb intended membrane lipids exclusively at select membrane contact sites. By conferring one additional condition to what is achievable with CID, CIT expands the types of manipulation in single live cells, to address cell biology questions otherwise intractable, and engineer cell functions for future synthetic biology applications.

Introduction

Chemically inducible dimerization (CID) uses a bifunctional small molecule to bring together two proteins with high affinity, specificity and fast kinetics^{1,2}. CID systems such as the rapamycin-dependent FKBP-FRB heterodimerization (Fig. 1a) exerts tight spatiotemporal control over local protein concentrations by oligomerization³ or by rapidly translocating a protein of interest to or from a desired site of action^{4,5}. Such strategies have enabled signal parsing of a given protein from the noise of other cell signaling pathways, leading to discoveries in cell migration, endocytosis, transcription, and translation^{1,2,6}. The seconds-to-minutes timescale offers a further advantage: CID strategies are less susceptible to genetic compensation that sometimes plague knockdown or knockout methods. When used as a building block for rewiring circuits in a bottom-up approach, CID systems have created fast, translation-independent synthetic logic gates in mammalian cells⁷. Over the years, CID has become a widely-used, easily generalizable chemical biology tool with promising clinical impact⁸.

While there have been hundreds of applications of CID, no rapidly inducible trimerization system has been developed to our knowledge. While the concept of trimerization has been demonstrated previously, for instance, with guide RNA as a trigger to trimerization of split Cas9 proteins and a specific DNA site⁹, we sought to develop a tool with modularity and broad applicability. Indeed, examples of transient or stable trimerization in biology exist, including but not limited to trimeric G proteins¹⁰, inner ear epithelial cell junctions¹¹, and MHC-antigen-TCR complexes governing T-cell selection¹². Engineering chemically inducible trimerization (CIT) could address biologically relevant questions, and expand the palette of what is achievable with chemical biology.

In theory, CIT should comprise of three unique protein components that can be brought together by a tri-functional small molecule. However, trimerization is difficult to achieve, as recruiting an additional protein doubles the possible bound states of the small molecule compared to dimerization (Supplementary Fig. 1). Efficient trimerization requires that the trimeric complex be the most favorable state over other less bound configurations. For efficient CID, positive cooperativity is essential: once a CID protein binds rapamycin, the resulting rapamycin-protein complex binds the second protein with > thousand-fold higher affinity than rapamycin alone¹³. This unique cooperativity is mediated through electrostatic interactions at the FKBP-rapamycin-FRB interface¹⁴. Because engineering *de novo* proteins with appropriate small molecule-dependent surface interactions should be highly challenging, we instead exploited the special properties of the FKBP-FRB CID system to achieve trimerization.

We present a novel CIT system whose components comprise split FRB and FKBP proteins (Fig. 1a). Candidate split proteins were computationally determined and characterized for their efficacy of trimerization in cells. Formation of the trimer *in vitro* was assessed by X-ray crystallography. CIT was used to target cytosolic proteins to inter-organellar membrane junctions and induce tri-organellar ER-plasma membrane-mitochondria contacts. Finally, we used CIT to locally alter phosphoinositide composition of ER-plasma membrane junctions. Altogether, CIT has small components that trimerize with fast kinetics in a rapamycin-inducible manner, expanding the variety of perturbations possible in the chemical biology toolkit.

Results

Design of split FRB and FKBP

We determined FRB and FKBP candidate split sites through rational design. We selected FRB (human mTOR residues 2021–2113) with a T2098L mutation, which makes it otherwise unstable unless bound to chemical ligands or FKBP¹⁵, to decrease recombination potential after protein splitting (Fig. 1b). FRB T2098L can also recognize rapamycin analogue AP21967, which unlike rapamycin does not bind MTOR pathways, and could be used in *in vivo* biological studies without toxicity^{16, 17}. In splitting FRB, we avoided its four alpha helices, crucial residues for FRB-FKBP-rapamycin stabilization (L2031, S2035, Y2038, F2039, T2098L, W2101, D2102, and Y2105)¹⁴, and regions of high conservation in the three FRB loops (Fig. 1c and Supplementary Fig. 2a,b). The SPELL algorithm¹⁸ was used to pinpoint candidate split sites in FRB through computational analysis. All loops selected for splitting (Fig. 1b,c and Supplementary Fig. 2a) show low evolutionary conservation with Kullback-Leibler conservation scores < 2 and have solvent accessible area values > 30 Å² (Fig. 1b)^{18,19,20}. Split energy profile determined by computing energy of the split parts relative to native energy of the intact protein (Fig. 1b) shows the three FRB loops residing in two major energy wells, which suggest FRB halves split at these sites are less likely to pre-associate¹⁸. Split sites for FKBP were also determined in this manner (Supplementary Fig. 4a,b). Hereafter, split FRB or FKBP proteins are abbreviated as sFRB or sFKBP. Each split site is numbered in terms of likelihood of success based on computational analysis; sFRB₁, sFRB₂ and sFRB₃ refer to pairs of sFRB proteins split at sites 1, 2 or 3, with split site 1 most likely to succeed. The N- or C-terminal half of a given sFRB protein pair is sFRB_{χN} or sFRB_{χC}, χ being the split site number.

We generated plasmids of N-terminal fluorophore-tagged sFRB proteins and observed cytosolic expression in transfected HeLa cells (Supplementary Fig. 2c). We also generated Lyn or CAAX tagged-sFRB fusion proteins, all of which correctly localized to the plasma membrane (PM) (Fig. 1d). To determine extent of possible pre-association between sFRB pairs, we used the Lyn motif to target sFRB_{χN} to the PM, and observed the localization of corresponding cytosolic sFRB_{χC} across all three split sites (χ = 1, 2, 3). Higher PM/cytosol ratios occurred between Lyn-Y-sFRB_{1N} and CFP-sFRB_{1C} compared to Lyn-Y-sFRB_{1N} and CFP alone (Fig. 1e,f 0.83 ± 0.01 vs. 0.75 ± 0.01, p < 0.0001). In contrast, cytosolic CFP-sFRB_{2N} and sFRB_{3N} PM/cytosol ratios did not differ from CFP alone (0.80 ± 0.01 vs. 0.77 ± 0.01, 0.82 ± 0.01 vs. 0.84 ± 0.01, respectively), suggesting the sFRB₁ pair has higher

tendency to pre-associate. This approach to designing split sites, validating cytosolic protein expression, and generating membrane-anchored protein was also applied to sFKBP.

Characterization of split FRB

The sFRB protein pairs were tested for their ability to bind FKBP in a rapamycin-inducible manner to achieve CIT. We co-expressed cytosolic FKBP with PM-localized sFRB pairs in HeLa cells. If functional, rapamycin would shift FKBP localization from the cytosol to the PM (Fig. 2a). sFRB pairs were localized to the PM with Lyn and CAAX tags (Fig. 1d). Upon rapamycin addition, all three sFRB pairs recruited mCh-FKBP to the PM, comparable to full length (FL) FRB (Fig. 2b). Changes in cell linescans reflect the cytosol-to-PM localization shift pre- and 9 mins post-rapamycin administration (Fig. 2b). Percent change in mCh-FKBP PM/cytosol ratios derived from linescans was positive for all sFRB pairs tested; values were not significantly different between sFRB₁, sFRB₂, and sFRB₃ and FL FRB (**p = 0.613, 0.057, 0.579 respectively**, Fig. 2c). However, no sFRB_C half could recruit FKBP to the PM without co-expression of its cognate sFRB_N half and vice versa ($p < 0.0001$ for all cases, Fig. 2c). These results suggest that with rapamycin addition, PM-localized sFRB halves are as efficient as full length FRB in recruiting FKBP, but each sFRB half cannot independently recruit FKBP. However, without FKBP overexpression, sFRB halves can still dimerize (Supplementary Fig. 3), as shown by rapamycin-dependent recruitment of cytosolic sFRB_{χC} to PM-localized Lyn-YFP-sFRB_{χN} ($\chi = 1, 2, 3$). This is most likely due to endogenous FKBP-rapamycin complexes in the cell²¹, and/or due to rapamycin alone bringing sFRB pairs together. sFKBP pairs were also screened, and 3 out of 4 split sites ($\chi = 1, 2, 3$) could recruit FRB (Fig. 3f and Supplementary Fig. 4).

Kinetics of cytosolic FKBP translocation to the PM was determined from exponential regression of cytosolic FKBP intensity decay. The rate constant of cytosolic FKBP signal decay with FL FRB was significantly higher than with the sFRB₁ pair ($0.085 \pm 0.0075 \text{ s}^{-1}$ versus $0.058 \pm 0.0047 \text{ s}^{-1}$, $p = 0.008$; Fig. 2d), indicating that sFRB₁ has slower FKBP recruitment kinetics after rapamycin addition. The timescale of FKBP recruitment by the sFRB₁ pair, however, still falls within the minutes range. To test for irreversibility, cells expressing PM-localized Lyn-YFP-sFRB_{χN}, cytosolic CFP-sFRB_{χC} ($\chi = 1, 2, 3$) and cytosolic mCh-FKBP were incubated with rapamycin for 30 mins. Samples were then washed 10x, and cells showing trimerization were imaged over 30 mins (Supplementary Fig. 5a). No appreciable decrease in PM/cytosol ratio was detected for either CFP-sFRB_χ or mCh-FKBP (Supplementary Fig. 5b), indicating that sFRB CIT systems are practically irreversible, similar to CID. To test for orthogonality, we assessed sFRB_N with sFRB_C halves split at different sites for rapamycin-based FKBP binding. sFRB pairs are non-orthogonal, but three additional sFRB pairs (sFRB_{1N}/sFRB_{3C}, sFRB_{2N}/sFRB_{1C}, sFRB_{2N}/sFRB_{3C}) were identified to trimerize with FKBP (Supplementary Fig. 6).

Structural validation of split FKBP

First, we solved the crystal structure of the FKBP12-rapamycin-FRB (T2098L) complex to examine whether the T2098L affects the overall conformation and/or the interaction with rapamycin. The crystal structure of FKBP12-rapamycin-FRB (T2098L) determined at 2.20 Å resolution (Fig. 3a) shows only 0.61 Å of the average root-mean-square

deviation (RMSD) for Ca atoms to the wild-type FRB-containing complex (PDB ID: 1FAP), indicating that the both structures are in almost perfect agreement. Also, the major interactions between FRB (T2098L), FKBP12 and rapamycin were the same as in the wild-type FRB-FKBP12-rapamycin complex (Fig. 3b). Hence, we confirmed that the T2098L mutation of FRB does not affect the overall conformation and the interactions with rapamycin.

Next, we attempted to purify sFRB χ and sFKBP χ fragments and reconstitute their complexes to structurally validate our split strategy. We could purify sFKBP_{1N} as an MBP fusion protein by an *E. coli* expression system although we could not obtain the sFRB χ_N fragments as a soluble protein. Therefore, we aimed to structurally validate whether sFKBP_{1N} and sFKBP_{1C} form a functional sFKBP₁ complex. First, we observed that sFKBP_{1N} and sFKBP_{1C} can form a stoichiometric sFKBP₁ complex at 10 μ M, dependent on the addition of rapamycin (Supplementary Fig. 7). We then solved crystal structures of sFKBP₁-rapamycin and sFKBP₁-rapamycin-FRB (T2098L) complexes at 2.92–3.11 Å resolution (Fig. 3c,d). In both structures, sFKBP_{1N} and sFKBP_{1C} formed the same secondary structure as FKBP12, showing only 0.38 and 0.42 Å of the average RMSD for Ca atoms to the corresponding region of the intact FKBP12 protein, respectively. The interactions between sFKBP₁ and rapamycin are completely conserved in both structures. Finally, the overall structure of sFKBP₁-rapamycin-FRB (T2098L) shows only 0.79 Å of the average RMSD to the intact FKBP12-rapamycin-FRB (T2098L) complex, without disrupting hydrogen bonds and major hydrophobic interactions to FRB and rapamycin (Fig. 3e). These results indicate that, *in vitro*, split FKBP fragments form a functional FKBP protein which is structurally indistinguishable to intact FKBP protein.

CIT at organelle membrane junction sites

Membrane contact sites (MCS) or junctions are regions of close inter-organelle membrane apposition where unique signaling can occur^{4,22,23}. MCS are widespread among almost all membrane-bound organelles^{24,25}, and local MCS molecular tethers and actuators²⁶ regulate processes ranging from calcium^{27,28,29} and lipid transport³⁰ to organelle fission^{31,32}. Most MCS regulate multiple functions, and local MCS proteins play compensatory roles, such that few MCS have been completely ablated by the knock-down or knock-out of a single gene³³. These confounding conditions make rapidly inducible perturbation attractive for studying MCS, as supported by prior studies^{4, 22, 23, 34}. As proof-of-principle, we used CIT to target cytosolic protein to ER-mitochondria and ER-PM MCS, demonstrating its potential as a generalizable recruitment-based screen for MCS function (Fig. 4a).

To recruit cytosolic protein to ER-PM junctions, we co-expressed PM-targeted sFRB_{1N} (Lyn-CFP-sFRB_{1N}) and ER-targeted sFRB_{1C} (YFP-sFRB_{1C}-Cb5) with cytosolic mCh-FKBP (Fig. 4a). After rapamycin addition, ER and PM tethering formed patches that colocalize with mCh-FKBP (Fig. 4b and Supplementary Video 1). Pairwise image correlation between all three image wavelengths all significantly increased after rapamycin ($p < 0.0001$, Fig. 4d), suggesting that the CIT system can recruit cytosolic protein to the ER-PM MCS. When we removed sFRB_{1N} (using Lyn-CFP only) or sFRB_{1C} (using only YFP-Cb5), trimerization could not be observed (Extended Data Fig. 1a,b, left and center)

with no increase in image correlation coefficients between all three signals. However, when mCh alone was expressed instead of mCh-FKBP, ER-PM tethering still occurred, albeit with no mCh recruitment to the site, and the image correlation coefficient between the ER and PM signals significantly increased (Extended Data Fig. 1a,b, right).

We also used sFKBP to recruit cytosolic FRB-mCh to ER-PM junctions. Cells showed undetectable or prominent FRB-mCh recruitment at ER-PM junctions pre- and 1 h post-rapamycin addition (Extended Data Fig. 2a,b, respectively). Imaging showed slower cytosolic protein recruitment compared to sFRB trimerization (12 mins vs. 1 h, Supplementary Video 1 vs. Supplementary Video 2). Pairwise image correlation significantly increased between ER and PM channels ($p < 0.0001$), cytosolic FRB-mCh and ER channels ($p = 0.030$), and not significantly between cytosolic FRB-mCh and PM channels ($p = 0.16$) (Extended Data Fig. 2c). Because sFKBP was less efficient compared to sFRB in targeting cytosolic proteins to ER-PM junctions, we decided to continue with only sFRB for MCS applications.

We also applied sFRB CIT to ER-mitochondria junctions. Complimentary sFRB pairs were expressed on the ER (sFRB_{1N}-CFP-Cb5) and mitochondria (Tom20-YFP-sFRB_{1C}), and post-rapamycin addition translocated mCh-FKBP to ER-mitochondria MCS (Fig. 4c and Supplementary Video 3). Pairwise image correlation coefficients increased for all three wavelengths, indicating successful trimerization ($p < 0.0001$ all cases; Fig. 4e). Likewise, removal of sFRB_{1N} (Lyn-YFP) and sFRB_{1C} (mCh-Cb5) yielded no translocation of mCh-FKBP to ER-mitochondria MCS after rapamycin addition (Extended Data Fig. 3a,b, left and center), whereas removal of FKBP resulted in increased co-localization between the ER and mitochondria components, without co-localization of mCh (Extended Data Fig. 3a,b, right).

CIT induces tri-organellar membrane contact sites

Multi-spectral imaging has revealed that ER-mitochondria MCS makes frequent contact with Golgi, peroxisomes, and lipid droplets, hinting at tri-organellar MCS²⁵. ER-mitochondria MCS also marks regions of autophagosome formation³⁵. We therefore speculated that a tri-organellar ER-PM-mitochondria junction site could exist due to the existence of ER-PM, ER-mitochondria, and PM-mitochondria MCS, and their shared function in Ca²⁺ signaling. Using CIT to determine if a tri-organellar junction could be synthetically formed between the PM, ER and mitochondria, we co-expressed sFRB_{1C} localized to the PM (Lyn-CFP-sFRB_{1C}), sFRB_{1N} to the ER (YFP-sFRB_{1N}-Cb5) and FKBP to the mitochondria (Tom20-mCh-FKBP) in Cos-7 cells (Fig. 5a-c). Fifteen minutes post-rapamycin addition, PM, ER and mitochondrial signals colocalized (Fig. 5b,c and Supplementary Video 4); all correlation coefficients increased ($p < 0.0001$; Fig. 5d). When sFRB_{1C}, sFRB_{1N}, or FKBP were each removed, trimerization no longer occurred post-rapamycin (Extended Data Fig. 4a,b, left and right), but removal of FKBP still resulted in colocalization of ER-PM signals (Extended Data Fig. 4a,b, center). These results show that CIT can induce PM-ER-mitochondria tethering, and serves as a detection method for potential tri-organellar MCS formation between three organelles.

Localized PI(4,5)P₂ depletion at ER-PM junctions

Functions of ER-PM MCS include Ca²⁺ re-entry and lipid homeostasis, with focus shifting to the latter in recent years³⁶. One major topic in the field is the regulation of secondary lipid messenger PI(4,5)P₂ (PIP₂) and its precursor PI(4)P. PM resident PIP₂ and its precursor PI(4)P levels are often in flux during signal transduction. ER-PM junctions serve as a bridge connecting the PM and ER, where local proteins regulate PM lipid homeostasis by using the ER as a reservoir or a sink, depending on the needs of the PM^{23, 34, 37}. While methods exist to perturb PM lipid composition or locally deplete PIP₂ from the PM³⁸, the means of perturbing lipids only at ER-PM junctions have yet to be established.

To achieve local PIP₂ depletion, we co-expressed PM-localized sFRB_{1N} (Lyn-Clover-FRB_{1N}), ER-localized sFRB_{1C} (iRFP-FRB_{1C}-Cb5), cytosolic CFP-FKBP fused to 5-phosphatase INP54P (331) (CF-INP54P), and PIP₂ biosensor mRuby-PH-PLC δ in Cos-7 cells (Fig. 6a). After rapamycin addition, CF-INP54P was recruited to ER-PM junctions, with a marked pattern of reduction in mRuby-PH-PLC δ intensity (Fig. 6b, left, and Supplementary Video 5). In contrast, recruitment of INP54P phosphatase-dead mutant CF-INP54P D281A, or CF alone did not reduce mRuby-PH-PLC δ intensity (Fig. 6b, center and left, and Supplementary Videos 6 and 7, respectively). Line-scan analysis (Fig. 6c) further confirmed the PIP₂ depletion confined to the ER-PM junctions (grey shades). Interestingly, PIP₂ levels in the regions outside ER-PM contact sites remained intact, accordingly forming a sharp gradient of PIP₂ immediately outside the junctions. Junctional PIP₂ reduction occurred in areas of high (teal dashed squares, Fig. 6b) compared to low ER-PM junction formation (orange dashed squares) 5 min after CF-INP54P recruitment by rapamycin, reflected in percent change in mRuby-PH-PLC δ intensity in the respective regions ($p < 0.0001$, Fig. 6d). CF-INP54P D281A recruitment to ER-PM rich regions only slightly decreased mRuby-PH-PLC δ intensity relative to outside these regions ($p = 0.0358$, Fig. 6d). CF recruitment to ER-PM rich regions did not significantly change mRuby-PH-PLC δ intensity compared to outside these regions ($p = 0.5189$, Fig. 6d). The same analysis conducted over time indicates that junctional PIP₂ reduction took place as early as 2 mins after INP54P recruitment with rapamycin (Extended Data Fig. 5), and with continued decrease in PIP₂ levels even after 10 mins. Lack of PIP₂ reduction in CF-INP54P D281A and CF controls further suggests that molecular crowding effects of CIT has minimal impact on the ability of mRuby-PH-PLC δ to detect PIP₂. These results collectively demonstrate that CIT-based recruitment of INP54P can locally deplete PIP₂ at ER-PM junctions.

Discussion

In this study we designed, developed and implemented the first known CIT system by rationally splitting proteins of the FKBP/FRB CID system. The CIT tool is small, robust, and trimerizes on a timescale of seconds-to-minutes. CIT responds to one chemical stimulus, and has clear trimeric stoichiometry according to crystallography results. We used CIT to rapidly target cytosolic protein exclusively to ER-PM and ER-mitochondria MCS, induce tri-organelle ER-mitochondria-PM junctions and locally deplete PIP₂ at ER-PM MCS. We believe that our ability to achieve CIT is attributed to the unique cooperativity of the

FKBP/FRB CID. This efficient CIT system would be otherwise highly difficult to achieve *de novo*, as engineering sequential cooperativity at protein interfaces would be necessary.

As FKBP binding affinity for rapamycin is over 10,000-fold higher than FRB (0.2 nM vs. 26 μ M)¹³, we believe that sFRB CIT is first achieved by formation of FKBP-rapamycin complexes, followed by sFRB halves binding. For the sFKBP system, our crystallization data show that rapamycin can dimerize sFKBP₁ halves in the absence of FRB. Gel filtration analysis indicates sFKBP₁ dimerizes saturatively at a protein concentration of 10 μ M in the presence of rapamycin (Supplementary Fig. 7), suggesting that the dissociation constant, switchable by rapamycin, between FKBP_{1N} and sFKBP_{1C} is less than a single digit micromolar concentration. We believe that in the sFKBP system, rapamycin brings together sFKBP with micromolar affinity, and then sFKBP-rapamycin complex recruits full length FRB. Our results suggest that the prevalent mechanism of trimerization for both sFRB and sFKBP CIT systems involves an initial complex formation of FKBP-rapamycin or sFKBP-rapamycin complexes, followed by the binding of sFRB or FRB respectively.

Components of sFRB and sFKBP CIT systems are small; sFRB_{1N} and sFRB_{1C} are 5 kDa and 6.3 kDa respectively. While sFRB _{χ N} and sFRB _{χ C} halves do not function orthogonally, we discovered three additional sFRB pairs (sFRB_{1N}/sFRB_{3C}, sFRB_{2N}/sFRB_{1C}, sFRB_{2N}/sFRB_{3C}) that trimerize with FKBP. In total, we generated 6 sFRB pairs capable of trimerization, increasing the likelihood of successful CIT implementation across biological systems. Further, the high degree of similarity between WT FRB and FRB T2098L in our crystallization data suggests that that WT or other FRB variants may be split similarly to generate additional CIT systems which respond to various rapamycin analogues.

Depletion of PIP₂ at ER-PM junctions (Fig. 6) catalyzes further investigation of local PIP₂ depletion at the ER-PM junction compared to global PIP₂ depletion at the PM; it may provide insight into the relationship between lipid transfer and Ca²⁺ entry at the ER-PM junction, as they share common players such as PIP₂ and PI(4)P. Additionally, the tri-organellar PM-ER-mitochondria junction formed through CIT indirectly suggests that these three organelles have the potential of interacting. In the future, CIT can be a powerful tool to validate and perturb other tri-organellar MCS, such as the ER-mitochondria-Golgi junction²⁵.

In all, we developed a trimerization tool capable of cell signaling manipulation in new ways. MCS targeting in this study demonstrated the enhanced spatiotemporal specificity CIT has over CID. We see potential for the tool beyond its role in future screens for studying MCS. Hundreds of available and validated CID-based actuators can now be readily retrofitted with CIT components to modulate various cell signaling pathways^{1, 2, 6}, including kinase modulation³⁹, and produce increasingly sophisticated, tunable switches and logic gates. Trimerization is also a common mechanism in nature, and CIT-based mimicry may deduce the significance of trimerization in these systems. By introducing a third component to be recruited to two others with one chemical stimulus, CIT introduces a new tool to chemical, synthetic and cell biology toolkits.

Online Methods

Cell culture and transfection

HeLa and Cos-7 cells were maintained at 37°C, 5% CO₂ and 95% humidity in Dulbecco's modified Eagle's medium (DMEM) supplemented with 10% FBS and 1% Pen/strep (Gibco). The day prior to imaging, cells were detached with 5% Trypsin-EDTA (Gibco) and harvested for reverse transfection with FuGENE HD (Promega). As a general rule, co-transfection of split and unsplit proteins used a split protein to unsplit protein plasmid ratio of 20:1 for sFRB CIT experiments and a ratio of 10:1 for sFKBP CIT. Prior to imaging, cell medium in samples was replaced with DPBS containing Ca²⁺ and Mg²⁺ for imaging < 30 mins or fresh DMEM growth media for imaging > 30 mins. Cells were transfected with constructs at adjusted relative plasmid ratios and incubated for 16-24h prior to imaging.

DNA plasmid construction

Constructs used to determine working split proteins were based off Clontech C1 and N1 backbones with various fluorophores. A 5xSAGG flexible linker oligo was annealed and inserted between KpnI and Sall restriction sites of both C1 and N1 backbones. Lyn or CAAX oligo DNA fragments were subsequently annealed and ligated into C1 or N1 backbones containing 5xSAGG linkers. Then, FRB or FKBP fragments were cloned and inserted between KpnI and BamHI or HindIII and Sall for C1 and N1 vectors respectively. To obtain non-Lyn or CAAX versions of the proteins, the portion containing fluorescent protein with split FRB or FKBP fragments were cut and pasted into C1 or N1 backbone vectors lacking Lyn or CAAX. YFP-sFRB_{1N}-Cb5 was generated by deletion mutagenesis of previously reported YFP-FRB-Cb5⁴. ER-targeting sequence Cb5 was amplified by PCR and subcloned into a sFRB_{1N}-C backbone from sFRB_{1N}-C-Cb5 to generate sFRB_{1N}-C-Cb5. CF-INP54P (331) and CF-INP54P (D281A) were from a previous report⁴⁰. All plasmids were verified by Sanger sequencing.

Live-cell imaging

Most imaging was conducted on a IX71 microscope (Olympus) with a 63x objective (and 1.6x zoom) and an ORCA-Flash4.0 LT Digital CMOS camera (Hamamatsu). Rate constant of FKBP recruitment by sFRB₁ was imaged at 10 s intervals with a spinning disc confocal, inverted Axiovert 200 (Zeiss) with a 40x objective and an Orca ER CCD camera (Hamamatsu). Both microscopes were driven by Metamorph 7.5 imaging software (Molecular Devices). Four-color imaging in Fig. 4 was conducted with an Eclipse Ti microscope (Nikon) with a 60x objective (and 1.5x zoom) and a Zyla 4.2 sCMOS camera (Andor), driven by NIS Elements software (Nikon). Unless otherwise indicated imaging was done at 1-3 min intervals for 12-30 mins, at times with between 3-5 0.5 um-spaced z positions. Images analyzed and shown are from a single plane, and not maximum intensity projections. Microscopy experiments applying CIT to membrane contact sites were conducted at 37°C, 5% CO₂ and humidity with a stage top incubation system (Tokai Hit).

Analysis of PM-to-cytosol ratio

PM-to-cytosol ratio was determined through line-scan analysis. Lines through cells were drawn to 1) avoid the nucleus and 2) maximize the two membrane signals on both sides of the cell. Two PM (p_1 , p_2) locations based on peak intensities (I) along the lines-can were determined visually. The cytosol was defined as midpoint location (m) between p_1 and p_2 . A moving average of 3 was used to determine signal intensity at p_1 and p_2 , and a moving average of 5 at the cytosol location. Then PM-to-cytosol ratio was determined for each PM location, and then averaged. Percent change was determined from PM to cytosol ratio values before and after rapamycin treatment.

$$\frac{PM}{cytosol} = \frac{5 \left(\sum_{p_1-1}^{p_1+1} I + \sum_{p_2-1}^{p_2+1} I \right)}{6 \sum_{m-2}^{m+2} I}$$

Analysis of recruitment rate

Averaged intensities from 3 regions of interest (ROI's) from the cytosol were used to generate exponential decay curves. Averaged intensity timepoints with exponential decay trends were selected for line fitting with an exponential regression to determine the exponential recruitment coefficient. R^2 values were all > 0.88 .

$$I = Ae^{-(rate\ constant)t}$$

Analysis of trimerization with Fisher's transform of Pearson's correlation coefficient

3 ROI's about 50 x 50 pixels were manually positioned for each cell to determine Pearson's correlation using FIJI. ROIs were chosen include enough background and organelle to mitigate false correlations. Due to organelle movement and deformation, different ROI's were selected for the same cell before and after rapamycin addition. Pairwise Pearson's correlation (between ROI1 and ROI2) was determined among three channels using the built-in MATLAB function `corr2`, and averaged between 3 ROI's. Fisher's transform was performed to normalize Pearson's correlation coefficient for later statistical analysis. The result is altogether referred to as correlation coefficient.

$$Correlation\ coefficient = \tanh^{-1}(corr2(ROI1, ROI2))$$

Statistical analysis and data visualization

Unless otherwise stated, most statistical analysis was done with unpaired, two-tailed Student's T-test assuming equal distributions. A paired, two-tailed Student's T-test was used in Fig. 6c. PRISM 6 software was used for statistical analysis and data visualization.

Split site prediction

Split sites were determined by selecting non-evolutionarily conserved solvent accessible loops. The Stride program⁴¹ was used to calculate the solvent accessible areas (SAA). Loops exceeding 30 Å² were selected as potential split sites. Sequence conservation as indicated by Kullback-Liebler conservation scores was determined with MISTIC⁴² and FKBP domain and FRB domain sequences used were obtained from PFAM server⁴³ (Finn 2014). Loops with Kullback-Leibler conservation scores less than 2 were selected as potential split sites. The difference between the native energy of the intact protein and the sum of the energies of the split proteins at a given split site - the split energy - was calculated using the MEDUSA scoring function⁴⁴ (Yin 2007). Energy wells were indicative of split sites in this study, which differs from the previous implementation of SPELL, which targeted regions outside energy wells⁴⁵. The original SPELL study looked for split proteins sites which minimized the destabilization as these proteins were then fused to a known destabilizer domain (iFKBP)⁴⁵. This approach ensures the prevention of the split part association in the absence of rapamycin.

Crystallography

Protein expression and purification

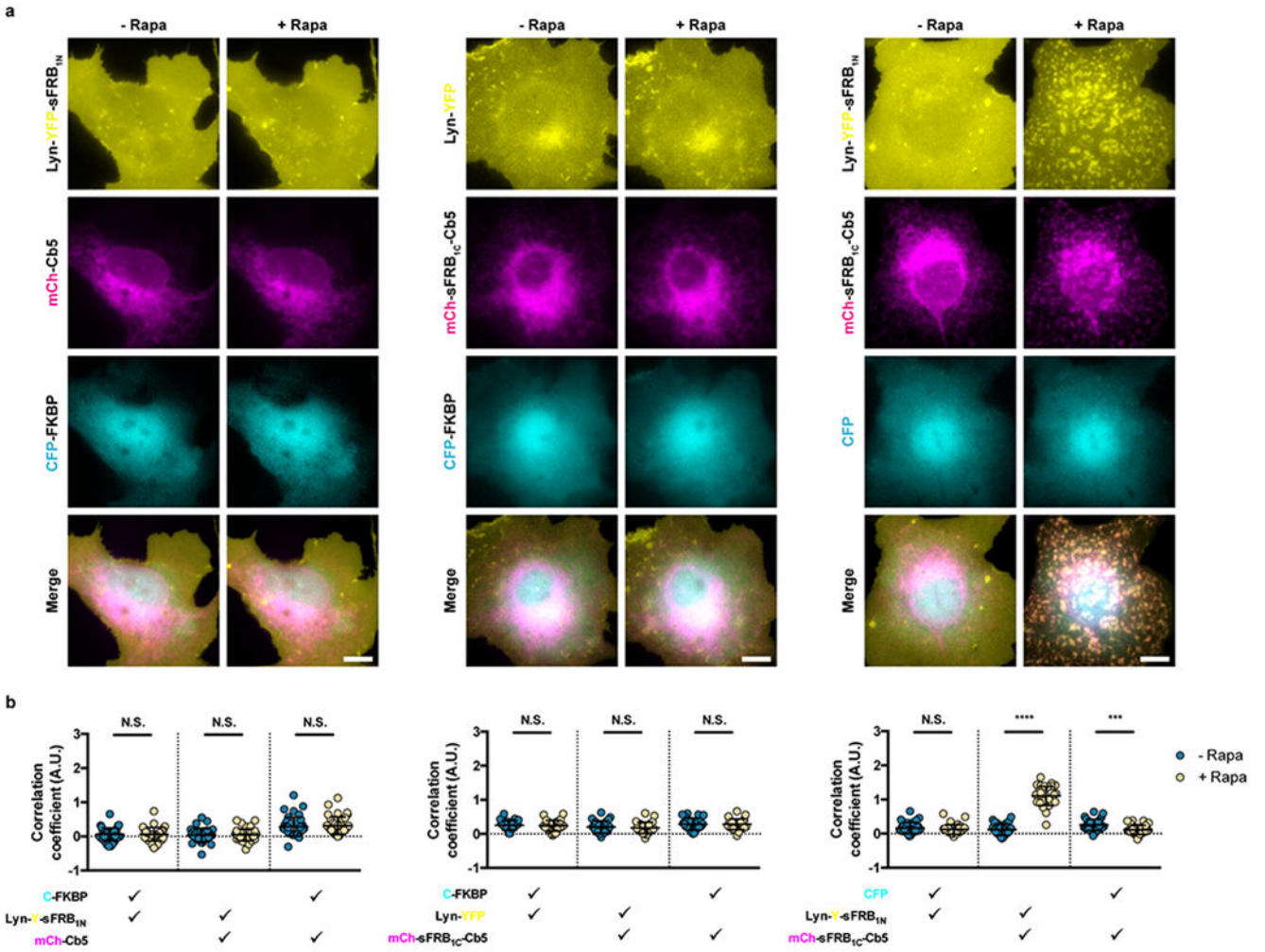
For structural analysis, cDNA encoding the sFKBP_{1N} (residues 1–32 of human FKBP12) was amplified by PCR and subcloned into a pET28a(+) derivative vector, which has a maltose binding protein (MBP)-encoding sequence inserted after an N-terminal polyhistidine tag. The construct contained a tobacco etch virus (TEV) protease recognition site at the junction between polyhistidine tag and the MBP sequences. Recombinant sFKBP_{1N} protein was expressed in *E. coli* BL21 (DE3) cells in LB broth at 37 °C until the OD₆₀₀ reached 0.8, at which point the temperature was shifted to 18 °C. Protein expression was induced by addition of isopropyl-β-D-thiogalactopyranoside to a final concentration of 250 μM. The cultures were grown for an additional 20 hrs and harvested by centrifugation. Cell pellets were resuspended in 50 mM Tris-HCl buffer (pH 7.0) containing 500 mM NaCl, 20 mM imidazole and 10% glycerol. Cells were lysed by sonication and clarified by centrifugation. The cell lysate was loaded onto a HisTrap HP column (GE Healthcare), and eluted with 50 mM Tris-HCl buffer (pH 7.0) containing 500 mM NaCl, 500 mM imidazole and 10% glycerol. The N-terminal histidine tag was cleaved by incubating with TEV protease overnight at 4 °C. The protein was further purified using a HiLoad Superdex 200 16/60 size-exclusion column (GE Healthcare) equilibrated with 20 mM Tris-HCl buffer (pH 8.0) containing 150 mM NaCl and 5 mM DTT. The sFKBP_{1C} (residues 33–108 of human FKBP12) was expressed and purified essentially as the same as sFKBP_{1N}, except an N-terminal His-SUMO tag was fused instead of the polyhistidine and MBP. The His-SUMO tag was cleaved by SUMO protease overnight at 4 °C. The purified sFKBP_{1N} and sFKBP_{1C} proteins were mixed in a 1:2 molar ratio, and then the mixture was added to a 1 μM rapamycin solution in 20 mM Tris-HCl buffer (pH 8.0) containing 150 mM NaCl, 5 mM DTT and 10% DMSO. The sFKBP_{1N}, sFKBP_{1C} and rapamycin mixture was filtered and loaded onto a Superdex 200 Increase 10/300 GL column (GE Healthcare) equilibrated with 20 mM Tris-HCl buffer (pH 8.0) containing 150 mM NaCl and 5 mM DTT. The eluted peak fractions of sFKBP₁-rapamycin complex were pooled and concentrated to 40 mg/ml.

For binding analysis, 100 μM MBP-sFKBP_{1N} and 10 μM SUMO-sFKBP_{1C} were mixed in 20 mM Tris-HCl buffer (pH 8.0) containing 150 mM NaCl, 5 mM DTT, and 10% DMSO in the presence or absence of 10 μM rapamycin. The samples were loaded on the Superdex 200 Increase 10/300 GL column, and fractions eluted around 13.8 and 15.4 ml were analyzed by SDS-PAGE. The cDNAs encoding human FKBP12 (residues 1–108) and FKBP12-rapamycin binding (FRB) domain encompassing residues 2021–2113 of human mTOR (T2098L) were subcloned into pET28a(+) containing an N-terminal polyhistidine-GST tag. The FKBP12 and FRB mutant proteins were expressed and purified essentially as the same as sFKBP_{1N}. The His-GST tag was cleaved by TEV protease overnight at 4 °C.

Crystallization, data collection and structure determination

Crystallization was performed by the sitting-drop vapor-diffusion method at 20 °C. Crystals of sFKBP₁-rapamycin appeared by mixing equal volumes of a 40 mg/ml sFKBP₁-rapamycin complex solution and a reservoir solution of 100 mM Na-HEPES buffer (pH 7.5) containing 20% (w/v) PEG 8000. FKBP12-rapamycin-FRB (T2098L) complex was prepared by mixing them at an equimolar ratio and incubating for 60 min on ice. Crystals of FKBP12-rapamycin-FRB (T2098L) appeared at 100 mM cacodylic acid buffer (pH 6.5) containing 350 mM zinc acetate and 8% (w/v) isopropanol. sFKBP₁-rapamycin-FRB (T2098L) complex was prepared in the same manner as FKBP12-rapamycin-FRB (T2098L). Crystals of sFKBP₁-rapamycin-FRB (T2098L) appeared at 100 mM Tris-HCl buffer (pH 7.0) containing 200 mM calcium acetate and 20% (w/v) PEG 3000. All crystals were briefly soaked in a cryoprotectant drop composed of the reservoir solution supplemented with 20% glycerol and then flash-cooled in liquid nitrogen for X-ray diffraction data collection. The datasets were collected at 1.000 Å, 100 K on the beamline BL26B2 at SPring-8 (Harima, Japan) or the beamline X06DA at the Swiss Light Source (Villigen, Switzerland). They were processed using the *XDS*⁴⁶ and scaled using *AIMLESS* supported by other programs of the *CCP4* suite⁴⁷. Crystal structures were determined by molecular replacement using *MOLREP*⁴⁸ with the FKBP12-rapamycin-FRB structure (PDB ID: 1FAP) and the MBP structure (PDB ID: 1ANF) as the search models. Model building was accomplished with *Coot*⁴⁹, and structural refinement was performed with *REFMAC*⁵⁰ and *PHENIX*⁵¹. The Ramachandran statistics are as follows: 96.0% favored, 4.0% allowed for sFKBP₁-rapamycin; 97.2% favored, 2.8% allowed for FKBP12-rapamycin-FRB (T2098L); and 96.8% favored, 3.2% allowed for sFKBP₁-rapamycin-FRB (T2098L). The data collection and refinement statistics are summarized in **Supplementary Table 1**. The structural models in the figures were depicted using *PyMOL* version 1.8 software (Schrödinger, LLC). Two-dimensional interaction plots were carried out with *LIGPLOT*⁵².

Extended Data



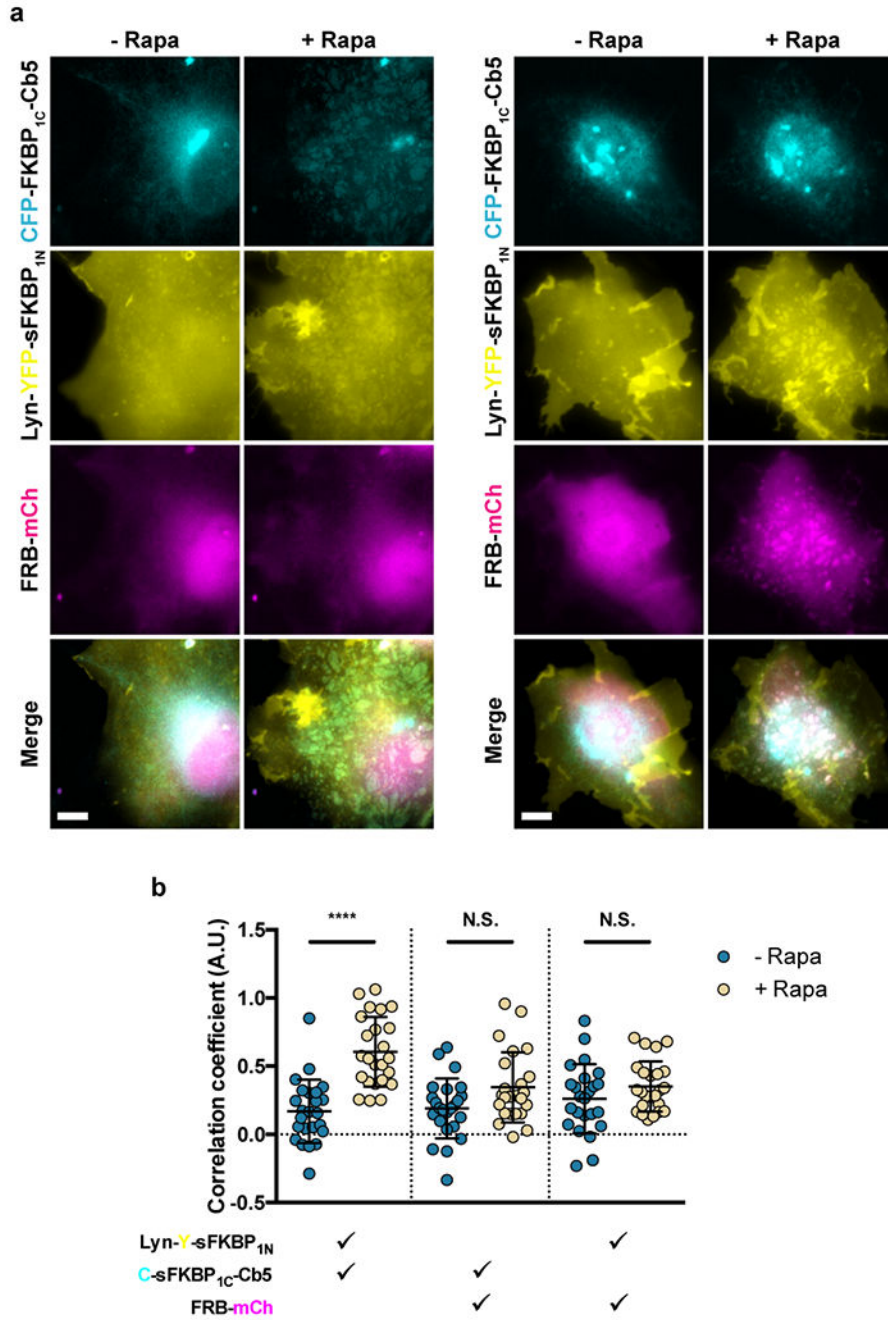
Extended Data Figure 1: Negative controls for cytosolic FKBP recruitment to ER-PM MCS.
 (a) Assessing contributions of each CIT component in CFP-FKBP recruitment to ER-PM MCS; left, middle and center panels correspond to constructs lacking ER, PM, and cytosolic CIT components. (b) Quantifying trimerization between the 3 signals pre- and post- 100 nM rapamycin. Check marks specify each combination of two wavelengths used in calculating pairwise Fisher’s transformation of Pearson’s correlation coefficients. Data are presented as mean values +/- SD. Two-tailed Student’s t-test assuming equal variance was used to compare correlations pre- and post-rapamycin. From left to right: $n = 38, 27,$ and 32 cells; 3 independent experiments each. Scalebar, $10 \mu\text{m}$. (***/****; $p < 0.001/0.0001$)

Author Manuscript

Author Manuscript

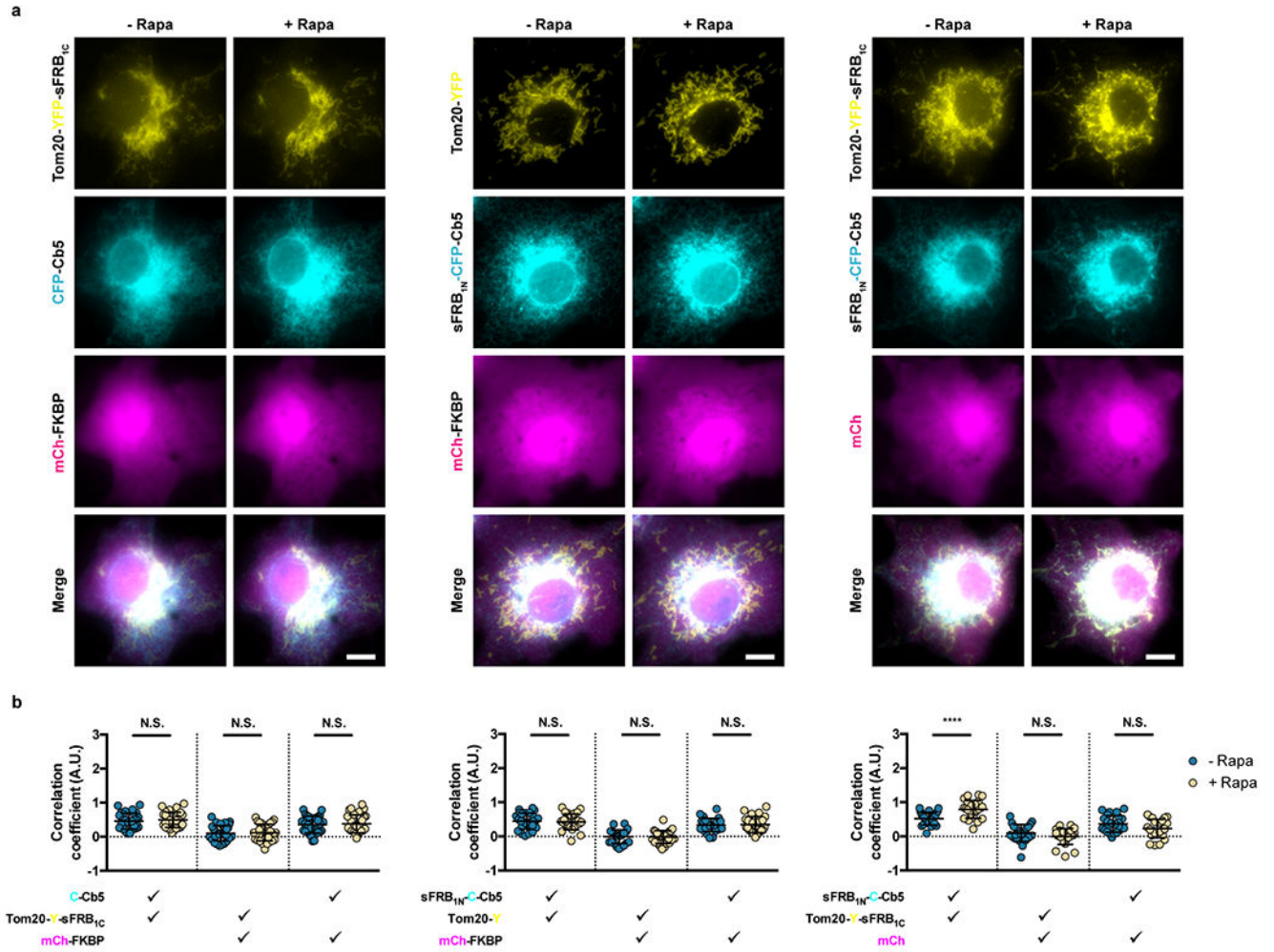
Author Manuscript

Author Manuscript



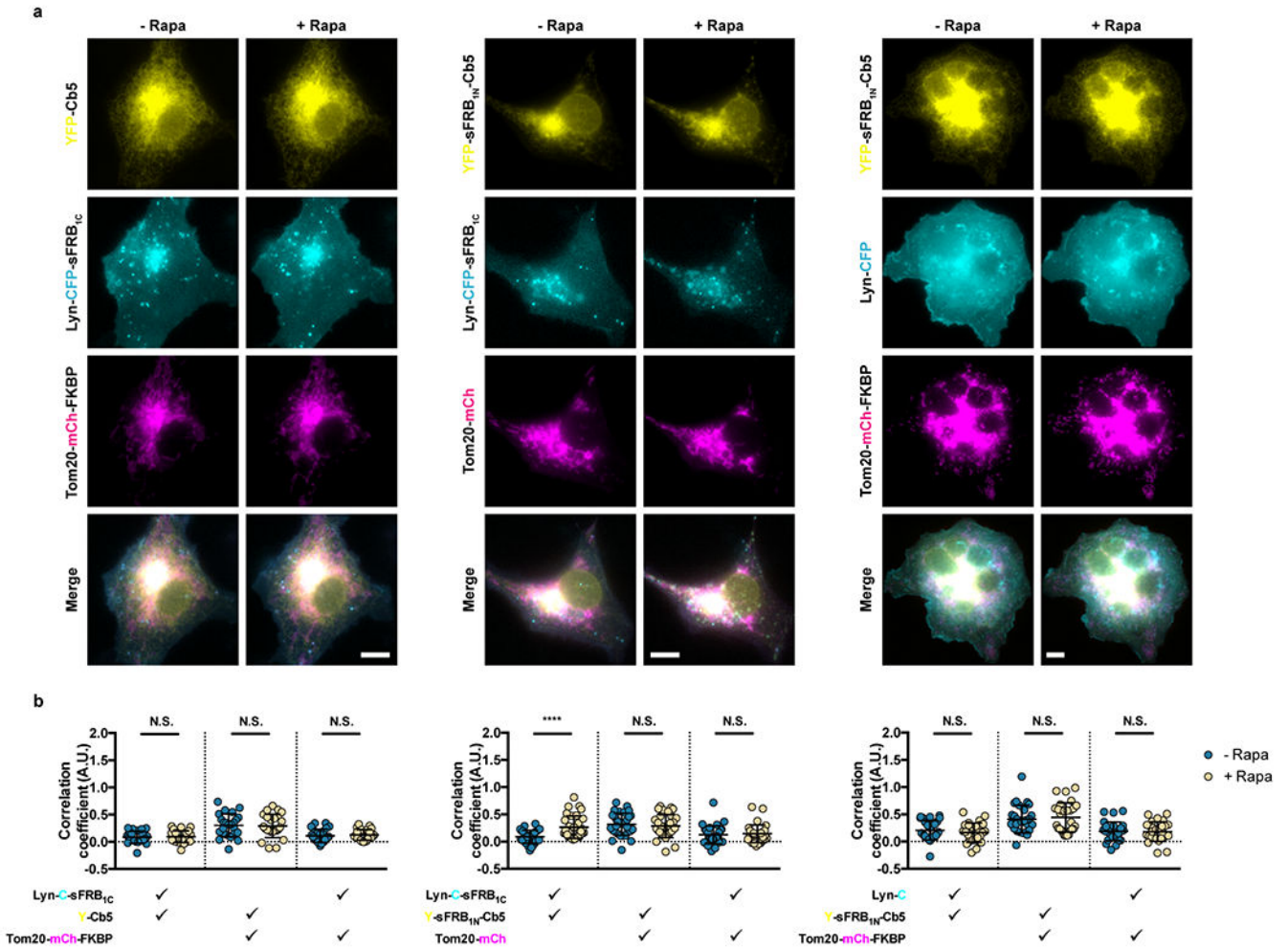
Extended Data Figure 2: sFKBP-based CIT recruitment of cytosolic FRB to ER-PM MCS. (a, b) Recruitment of mCh-FRB to ER-PM junctions by ER and PM targeted sFKBP_{1N} and sFKBP_{1C}, pre- and 1 h post- 100 nM rapamycin addition. FRB-mCh recruitment can be (a) undetectable or (b) prominent. (c) Quantifying trimerization between the 3 signals pre- and post-rapamycin. Check marks specify each combination of two wavelengths used in calculating pairwise Fisher's transformation of Pearson's correlation coefficients. Data are presented as mean values \pm SD. Two-tailed Student's t-test assuming equal variance was

used to compare correlations pre- and post- rapamycin. From left to right: $n = 24$ cells; 3 independent experiments each. Scalebar, 10 μm . (****; $p < 0.0001$)



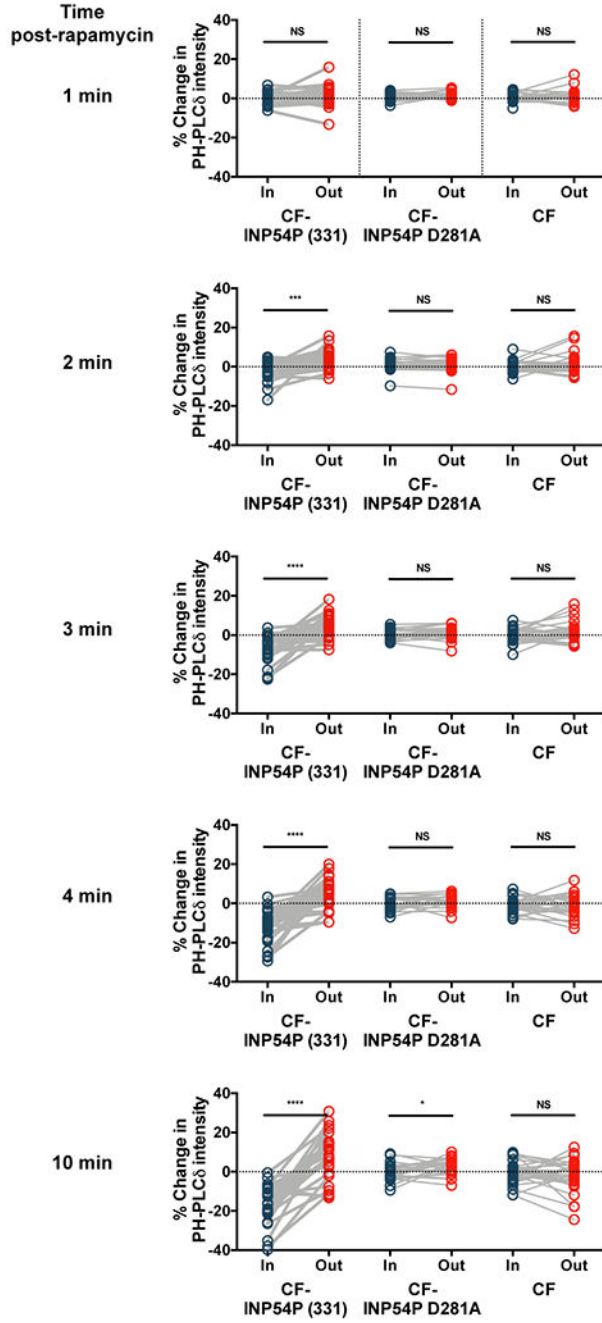
Extended Data Figure 3: Negative controls for cytosolic FKBP recruitment to ER-mitochondria MCS.

(a) Assessing contributions of each CIT component in CFP-FKBP recruitment to ER-mitochondria MCS; left, middle and center panels correspond to constructs lacking ER, mitochondria, and cytosolic CIT components. (b) Quantifying trimerization between the 3 signals pre- and post- 100 nM rapamycin. Check marks specify each combination of two wavelengths used in calculating pairwise Fisher’s transformation of Pearson’s correlation coefficients. Data are presented as mean values \pm SD. Two-tailed Student’s t-test assuming equal variance was used to compare correlations pre- and 12 mins post- rapamycin. From left to right: $n = 32, 26,$ and 24 cells; 3 independent experiments each. Scalebar, 10 μm . (****; $p < 0.0001$)



Extended Data Figure 4: Negative controls for CIT-induced ER-mitochondria-PM tri-organelle membrane contact sites (MCS).

(a) Assessing contributions of each CIT component in tri-organelle MCS formation; left, middle and center panels correspond to constructs lacking ER, mitochondria, and PM CIT components. (b) Quantifying trimerization between the 3 signals pre- and post- 100 nM rapamycin. Check marks specify each combination of two wavelengths used in calculating pairwise Fisher's transformation of Pearson's correlation coefficients. Data are presented as mean values \pm SD. Two-tailed Student's t-test assuming equal variance was used to compare correlations pre- and 15 mins post-rapamycin. From left to right: $n = 24, 32$ and 28 cells; 3 independent experiments each. Scalebar, 10 μm . (****, $p < 0.0001$)



Extended Data Figure 5: PIP₂ biosensor intensity at ER-PM junction sites over time. Intensities of mRuby PH-PLCδ PIP₂ biosensor of user defined regions of interest inside and outside ER-PM MCS at 1, 2, 3, 4 and 10 min after 100 nM rapamycin. Significance analyzed with two-tailed paired Students t-tests assuming equal variance. From left to right: *n* = 28, 25 and 23 cells; 4 independent experiments each. (*/***/****; *p* < 0.05/0.001/0.0001)

Supplementary Material

Refer to Web version on PubMed Central for supplementary material.

Acknowledgements

We thank Luca Bertozzi and Sarah Thompson for help with plasmid generation. We thank Robert DeRose, Xinyi Y. Zhou, and Yuta Nihongaki for proofreading the manuscript. We thank Hideaki Niwa (RIKEN), Naoki Sakai (RIKEN), and the staff at the BL26B2 beamline (Proposal No. 20190047) of SPring-8 (Harima, Japan) and the X06DA beamline (Proposal No. 20171001) of the Swiss Light Source, Paul Scherrer Institut (Villigen, Switzerland) for their help in X-ray diffraction data collection. We acknowledge support from the National Institutes for Health (5R01GM123130 to T.I., and 5R01GM123247 and 1R35 GM134864 to N.V.D.), the Passan Foundation to N.V.D., the DoD DARPA (HR0011-16-C-0139 to T.I.), and the PRESTO program of the Japan Science and Technology Agency to T.U. (No. JPMJPR12A3) and T.I (No. JPMJPR12A5), and a Grant-in-Aid for Scientific Research (B) to T.U. (No. 16H05089) from the Japan Society for the Promotion of Science.

Data Availability

The data that support the findings of this study are available from the corresponding authors upon reasonable request.

References

1. Fegan A, White B, Carlson JC & Wagner CR Chemically controlled protein assembly: techniques and applications. *Chem Rev* 110, 3315–3336 (2010). [PubMed: 20353181]
2. DeRose R, Miyamoto T & Inoue T Manipulating signaling at will: chemically-inducible dimerization (CID) techniques resolve problems in cell biology. *Pflugers Arch* 465, 409–417 (2013). [PubMed: 23299847]
3. Spencer DM, Wandless TJ, Schreiber SL & Crabtree GR Controlling signal transduction with synthetic ligands. *Science* 262, 1019–1024 (1993). [PubMed: 7694365]
4. Komatsu T et al. Organelle-specific, rapid induction of molecular activities and membrane tethering. *Nat Methods* 7, 206–208 (2010). [PubMed: 20154678]
5. Haruki H, Nishikawa J & Laemmli UK The anchor-away technique: rapid, conditional establishment of yeast mutant phenotypes. *Mol Cell* 31, 925–932 (2008). [PubMed: 18922474]
6. Putyrski M & Schultz C Protein translocation as a tool: The current rapamycin story. *FEBS Lett* 586, 2097–2105 (2012). [PubMed: 22584056]
7. Miyamoto T et al. Rapid and orthogonal logic gating with a gibberellin-induced dimerization system. *Nat Chem Biol* 8, 465–470 (2012). [PubMed: 22446836]
8. Stanton BZ, Chory EJ & Crabtree GR Chemically induced proximity in biology and medicine. *Science* 359 (2018).
9. Ma D, Peng S & Xie Z Integration and exchange of split dCas9 domains for transcriptional controls in mammalian cells. *Nat Commun* 7, 13056 (2016). [PubMed: 27694915]
10. Lambright DG et al. The 2.0 Å crystal structure of a heterotrimeric G protein. *Nature* 379, 311–319 (1996). [PubMed: 8552184]
11. Higashi T & Miller AL Tricellular junctions: how to build junctions at the TRICKiest points of epithelial cells. *Mol Biol Cell* 28, 2023–2034 (2017). [PubMed: 28705832]
12. Hennecke J & Wiley DC T cell receptor-MHC interactions up close. *Cell* 104, 1–4 (2001). [PubMed: 11163234]
13. Banaszynski LA, Liu CW & Wandless TJ Characterization of the FKBP.rapamycin.FRB ternary complex. *J Am Chem Soc* 127, 4715–4721 (2005). [PubMed: 15796538]
14. Choi J, Chen J, Schreiber SL & Clardy J Structure of the FKBP12-rapamycin complex interacting with the binding domain of human FRAP. *Science* 273, 239–242 (1996). [PubMed: 8662507]
15. Stankunas K et al. Rescue of degradation-prone mutants of the FK506-rapamycin binding (FRB) protein with chemical ligands. *Chembiochem* 8, 1162–1169 (2007). [PubMed: 17525916]

16. Liberles SD, Diver ST, Austin DJ & Schreiber SL Inducible gene expression and protein translocation using nontoxic ligands identified by a mammalian three-hybrid screen. *Proc Natl Acad Sci U S A* 94, 7825–7830 (1997). [PubMed: 9223271]
17. Bayle JH et al. Rapamycin analogs with differential binding specificity permit orthogonal control of protein activity. *Chem Biol* 13, 99–107 (2006). [PubMed: 16426976]
18. Dagliyan O et al. Computational design of chemogenetic and optogenetic split proteins. *Nat Commun* 9, 4042 (2018). [PubMed: 30279442]
19. Dagliyan O et al. Engineering extrinsic disorder to control protein activity in living cells. *Science* 354, 1441–1444 (2016). [PubMed: 27980211]
20. Dagliyan O, Dokholyan NV & Hahn KM Engineering proteins for allosteric control by light or ligands. *Nat Protoc* 14, 1863–1883 (2019). [PubMed: 31076662]
21. Belshaw PJ, Schoepfer JG, Liu KQ, Morrison KL & Schreiber SL Rational Design of Orthogonal Receptor-Ligand Combinations. *Angewandte Chemie-International Edition in English* 34, 2129–2132 (1995).
22. Varnai P, Toth B, Toth DJ, Hunyady L & Balla T Visualization and manipulation of plasma membrane-endoplasmic reticulum contact sites indicates the presence of additional molecular components within the STIM1-Orai1 Complex. *J Biol Chem* 282, 29678–29690 (2007). [PubMed: 17684017]
23. Dickson EJ et al. Dynamic formation of ER-PM junctions presents a lipid phosphatase to regulate phosphoinositides. *J Cell Biol* 213, 33–48 (2016). [PubMed: 27044890]
24. Phillips MJ & Voeltz GK Structure and function of ER membrane contact sites with other organelles. *Nat Rev Mol Cell Biol* 17, 69–82 (2016). [PubMed: 26627931]
25. Valm AM et al. Applying systems-level spectral imaging and analysis to reveal the organelle interactome. *Nature* 546, 162–167 (2017). [PubMed: 28538724]
26. Prinz WA Bridging the gap: membrane contact sites in signaling, metabolism, and organelle dynamics. *J Cell Biol* 205, 759–769 (2014). [PubMed: 24958771]
27. Luik RM, Wang B, Prakriya M, Wu MM & Lewis RS Oligomerization of STIM1 couples ER calcium depletion to CRAC channel activation. *Nature* 454, 538–542 (2008). [PubMed: 18596693]
28. Liou J et al. STIM is a Ca²⁺ sensor essential for Ca²⁺-store-depletion-triggered Ca²⁺ influx. *Curr Biol* 15, 1235–1241 (2005). [PubMed: 16005298]
29. Rizzuto R et al. Close contacts with the endoplasmic reticulum as determinants of mitochondrial Ca²⁺ responses. *Science* 280, 1763–1766 (1998). [PubMed: 9624056]
30. Levine T & Loewen C Inter-organelle membrane contact sites: through a glass, darkly. *Curr Opin Cell Biol* 18, 371–378 (2006). [PubMed: 16806880]
31. Friedman JR et al. ER tubules mark sites of mitochondrial division. *Science* 334, 358–362 (2011). [PubMed: 21885730]
32. Rowland AA, Chitwood PJ, Phillips MJ & Voeltz GK ER contact sites define the position and timing of endosome fission. *Cell* 159, 1027–1041 (2014). [PubMed: 25416943]
33. Helle SC et al. Organization and function of membrane contact sites. *Biochim Biophys Acta* 1833, 2526–2541 (2013). [PubMed: 23380708]
34. Zewe JP, Wills RC, Sangappa S, Goulden BD & Hammond GR SAC1 degrades its lipid substrate PtdIns4P in the endoplasmic reticulum to maintain a steep chemical gradient with donor membranes. *Elife* 7 (2018).
35. Hamasaki M et al. Autophagosomes form at ER–mitochondria contact sites. *Nature* 495, 389–393 (2013). [PubMed: 23455425]
36. Saheki Y & De Camilli P Endoplasmic Reticulum-Plasma Membrane Contact Sites. *Annu Rev Biochem* 86, 659–684 (2017). [PubMed: 28301744]
37. Chang CL & Liou J Phosphatidylinositol 4,5-Bisphosphate Homeostasis Regulated by Nir2 and Nir3 Proteins at Endoplasmic Reticulum-Plasma Membrane Junctions. *J Biol Chem* 290, 14289–14301 (2015). [PubMed: 25887399]
38. Idevall-Hagren O, Dickson EJ, Hille B, Toomre DK & De Camilli P Optogenetic control of phosphoinositide metabolism. *Proc Natl Acad Sci U S A* 109, E2316–2323 (2012). [PubMed: 22847441]

39. Karginov AV, Ding F, Kota P, Dokholyan NV & Hahn KM Engineered allosteric activation of kinases in living cells. *Nat Biotechnol* 28, 743–747 (2010). [PubMed: 20581846]
40. Suh BC, Inoue T, Meyer T & Hille B Rapid chemically induced changes of PtdIns(4,5)P₂ gate KCNQ ion channels. *Science* 314, 1454–1457 (2006). [PubMed: 16990515]
41. Heinig M & Frishman D STRIDE: a web server for secondary structure assignment from known atomic coordinates of proteins. *Nucleic Acids Research* 32, W500–W502 (2004). [PubMed: 15215436]
42. Colell EA, Iserte JA, Simonetti FL & Marino-Buslje C MISTIC2: comprehensive server to study coevolution in protein families. *Nucleic Acids Research* 46, W323–W328 (2018). [PubMed: 29905875]
43. Finn RD et al. Pfam: the protein families database. *Nucleic Acids Research* 42, D222–D230 (2014). [PubMed: 24288371]
44. Yin SY, Ding F & Dokholyan NV Eris: an automated estimator of protein stability. *Nature Methods* 4, 466–467 (2007). [PubMed: 17538626]
45. Dagliyan O et al. Computational design of chemogenetic and optogenetic split proteins. *Nature Communications* 9 (2018).
46. Kabsch W Automatic Processing of Rotation Diffraction Data from Crystals of Initially Unknown Symmetry and Cell Constants. *J Appl Crystallogr* 26, 795–800 (1993).
47. Winn MD et al. Overview of the CCP4 suite and current developments. *Acta Crystallogr D* 67, 235–242 (2011). [PubMed: 21460441]
48. Vagin A & Teplyakov A Molecular replacement with MOLREP. *Acta Crystallographica Section D-Biological Crystallography* 66, 22–25 (2010).
49. Emsley P, Lohkamp B, Scott WG & Cowtan K Features and development of Coot. *Acta Crystallographica Section D-Biological Crystallography* 66, 486–501 (2010).
50. Murshudov GN, Vagin AA & Dodson EJ Refinement of macromolecular structures by the maximum-likelihood method. *Acta Crystallogr D* 53, 240–255 (1997). [PubMed: 15299926]
51. Adams PD et al. PHENIX: a comprehensive Python-based system for macromolecular structure solution. *Acta Crystallogr D* 66, 213–221 (2010). [PubMed: 20124702]
52. Laskowski RA & Swindells MB LigPlot+: multiple ligand-protein interaction diagrams for drug discovery. *J Chem Inf Model* 51, 2778–2786 (2011). [PubMed: 21919503]

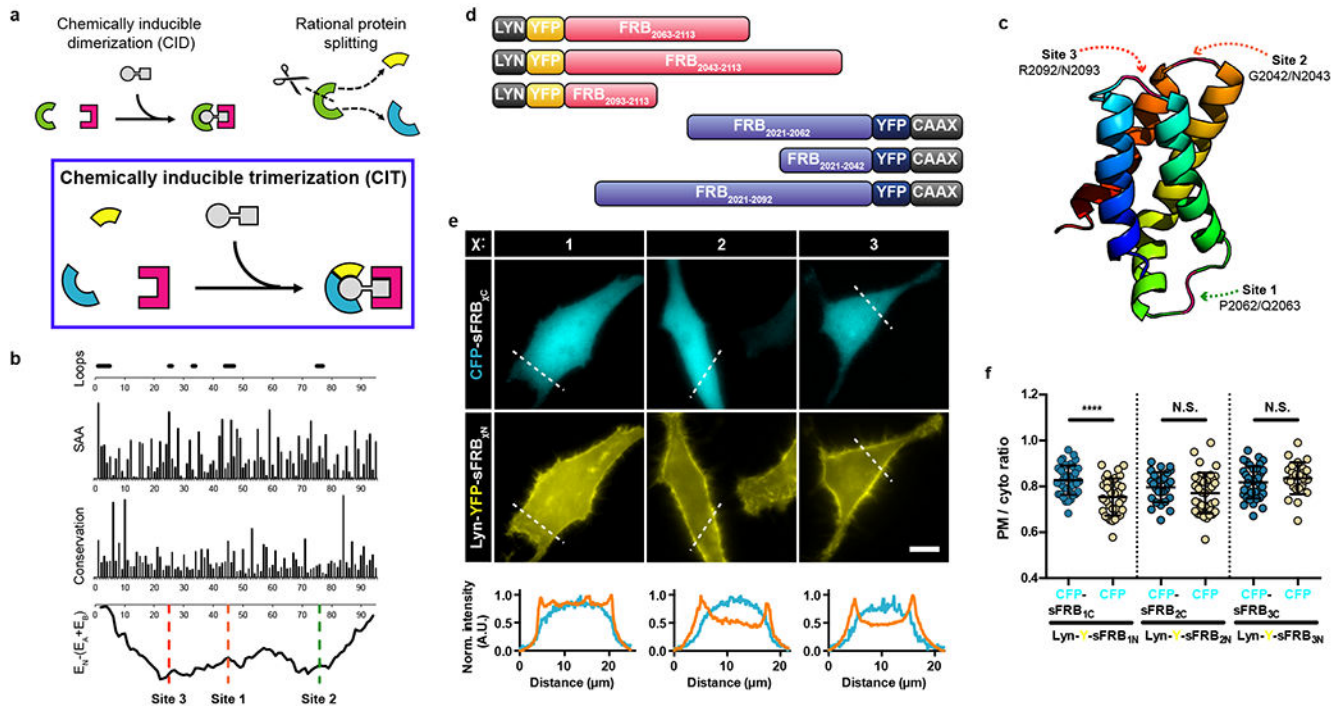


Figure 1: Rational CIT design and sFRB overexpression in cells.

(a) CID proteins FRB (green arc) sites generates FRB protein halves (yellow and blue). Split FRB halves and FKBP form three components of CIT. Rapamycin brings them together.

(b) Computationally analysis to determine split sites for FRB domain only. Loop areas with high solvent accessibility area (SAA), low conservation and favorable split energy profiles were chosen.

(c) FRB structure (PDB ID: 1AUE) consists of 4 α -helices; split sites 1, 2 and 3 all reside in linker regions between α -helices.

(d) Examples of sFRB fusion protein design. Lyn or CAAX motifs target sFRBs to the PM. (e) Co-overexpression of sFRB protein pairs in HeLa cells. N-terminal sFRB halves (sFRB_{1N}, sFRB_{2N}, sFRB_{3N}) are PM localized by Lyn and C-terminal sFRB halves (sFRB_{1C}, sFRB_{2C}, sFRB_{3C}) are cytosolic.

Linescans below show normalized PM (orange) and cytosolic (blue) signal intensity. (f) Pre-association between sFRB halves. PM-to-cytoplasmic ratios derived from linescans of cytosolic sFRB_{1C}, sFRB_{2C}, and sFRB_{3C} co-expressed with PM-targeted sFRB_{1N}, sFRB_{2N}, and sFRB_{3N} respectively compared to CFP alone. Data are presented as mean values \pm SD. From left to right: 39, 33, 27, 39, 36, and 26 cells; 3 independent experiments each.

Two-tailed Student's t test assuming equal variance was used, p-values indicated in graph.

Scale bar, 10 μ m.

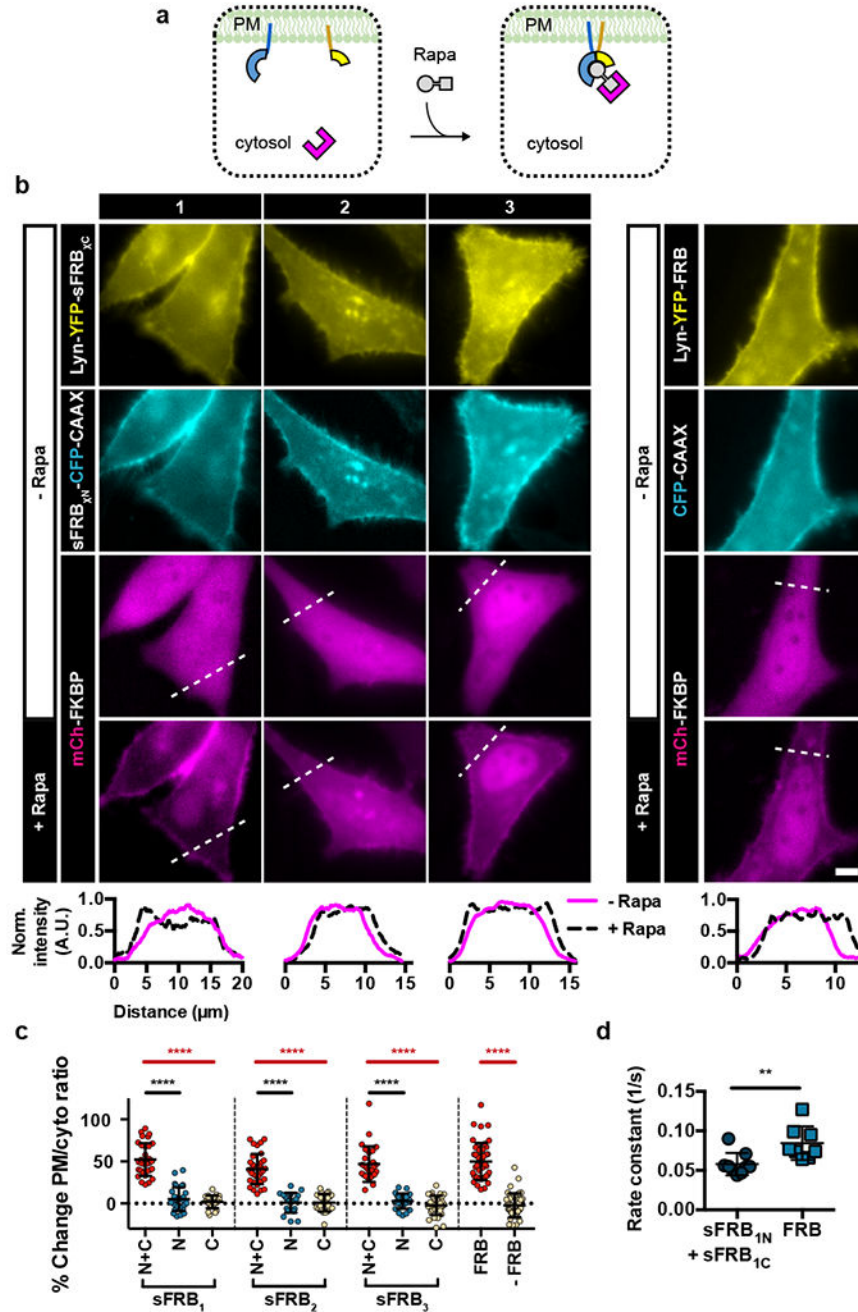


Figure 2: Characterization of FKBP recruitment extent and kinetics by sFRB after rapamycin addition.
 (a) Experimental setup for FKBP recruitment efficacy by sFRBs. sFRB N-terminal and C-terminal halves are PM-targeted by CAAX or Lyn respectively and co-expressed with FKBP. Cytosol-to-PM translocation by FKBP indicates successful recruitment. (b) Translocation of FKBP from cytosol to PM in HeLa cells co-expressing PM-targeted sFRB₁, sFRB₂, sFRB₃ pairs and full length FRB. Pre-rapamycin; top 3 rows. 9 min post-rapamycin; bottom row. Linescans show corresponding normalized intensity of mCh-FKBP signal. (c) Percent change in mCh-FKBP PM-to-cytoplasmic ratio pre- and post-rapamycin addition.

FKBP recruitment by sFRB pairs (N + C) compared to N or C-terminal halves only (N or C), full length FRB or no FRB in FKBP recruitment. Data are presented as mean values \pm SD. From left to right: $n = 31, 29, 24, 34, 20, 24, 27, 23, 34, 47,$ and 43 cells; 3-6 independent experiments each. Two-tailed Student's t-test assuming equal variance was used, p-values indicated in graph. (d) FKBP recruitment rate constants derived from exponential regression of cytosolic FKBP signal decay imaged with confocal microscopy over 10 s intervals. sFRB_{1C} + sFRB_{1N} and FRB groups use identical plasmid constructs as leftmost and rightmost columns respectively in (b). Data are presented as mean values \pm SD. From left to right: $n = 9$ and 8 cells; 4-5 independent experiments each. Two-tailed Student's t-test assuming equal variance was used, p-values indicated in graph. Scale bar, 5 μm .

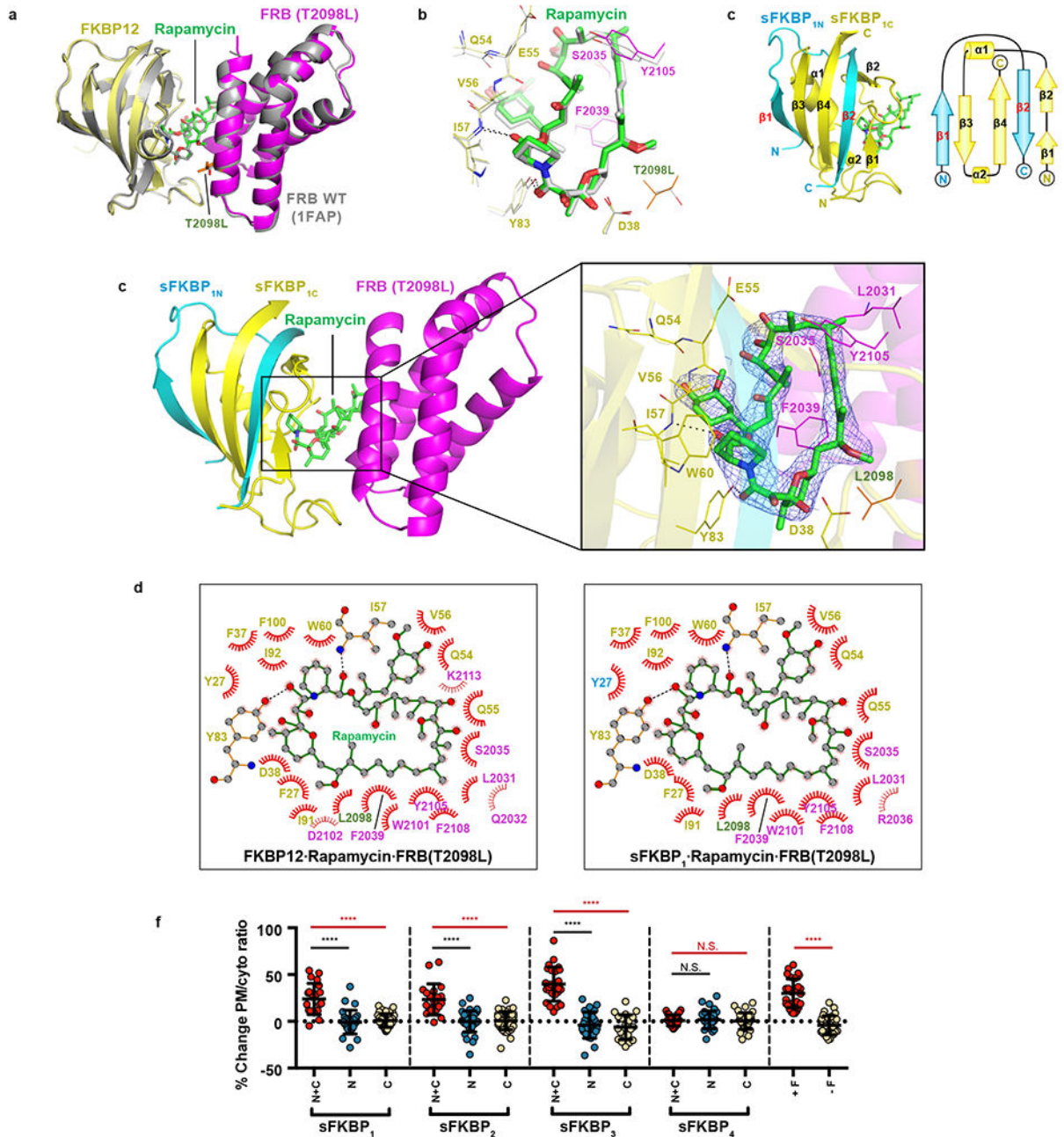


Figure 3: Crystal structure of the split and unsplit FKBP-rapamycin-FRB (T2098L) complexes
 (a) Superimposition of FKBP12-rapamycin-FRB (T2098L) complex crystal structure (yellow, green and magenta) with that of FKBP12-rapamycin-FRB (wild type; PDB ID: 1FAP, gray). T2098L is shown in orange. (b) Zoom-in view of the rapamycin-interacting region of FKBP12-rapamycin-FRB complexes (color-coded as in panel a). Hydrogen bonds are shown as dashes. (c) Ribbon (left) and topology (right) diagrams of the sFKBP_{1N} (cyan), FKBP_{1C} (yellow) and rapamycin (green) complex. (d) Crystal structure of sFKBP₁-rapamycin-FRB (T2098L). Left, sFKBP₁ (cyan and yellow), rapamycin (green)

and FRB (T2098L, magenta) is depicted as a ribbon diagram. Right, Electron density of rapamycin. Rapamycin is depicted as a stick model with a 2Fo-Fc electron density (blue mesh) contoured at 1.5σ . Residues of sFKBP_{1C} (yellow) and FRB (T2098L) (magenta) involved in the interaction with rapamycin are labeled and shown as a line model. (e) LIGPLOT diagrams showing critical contacts around rapamycin. Left, FKBP12-rapamycin-FRB (T2098L). Right, sFKBP₁-rapamycin-FRB (T2098L). Rapamycin (green) and key residues of unsplit (left) and split (right) FKBP proteins (yellow; Y27 of sFKBP_{1N} in cyan) and those of FRB (magenta; T2098L in orange) are depicted in a ball and stick model. Carbon, nitrogen and oxygen are gray, blue and red balls, respectively. Hydrogen bond and hydrophobic interaction is shown in a black dashed line and a red arc of a circle, respectively. (f) Percent change in FRB-mCh PM-to-cytosolic ratio pre- and post-rapamycin addition. Each sFKBP pair (N + C) is compared with N or C-terminal halves only (N or C), full length FKBP or no FKBP in FRB recruitment. Data are presented as mean values \pm SD. From left to right: n = 21, 28, 38, 20, 39, 38, 25, 25, 21, 28, 32, 33, 29 and 31 cells; 3 – 13 independent experiments each. Two-tailed Student's t-test assuming equal variance used, p-values indicated in graph.

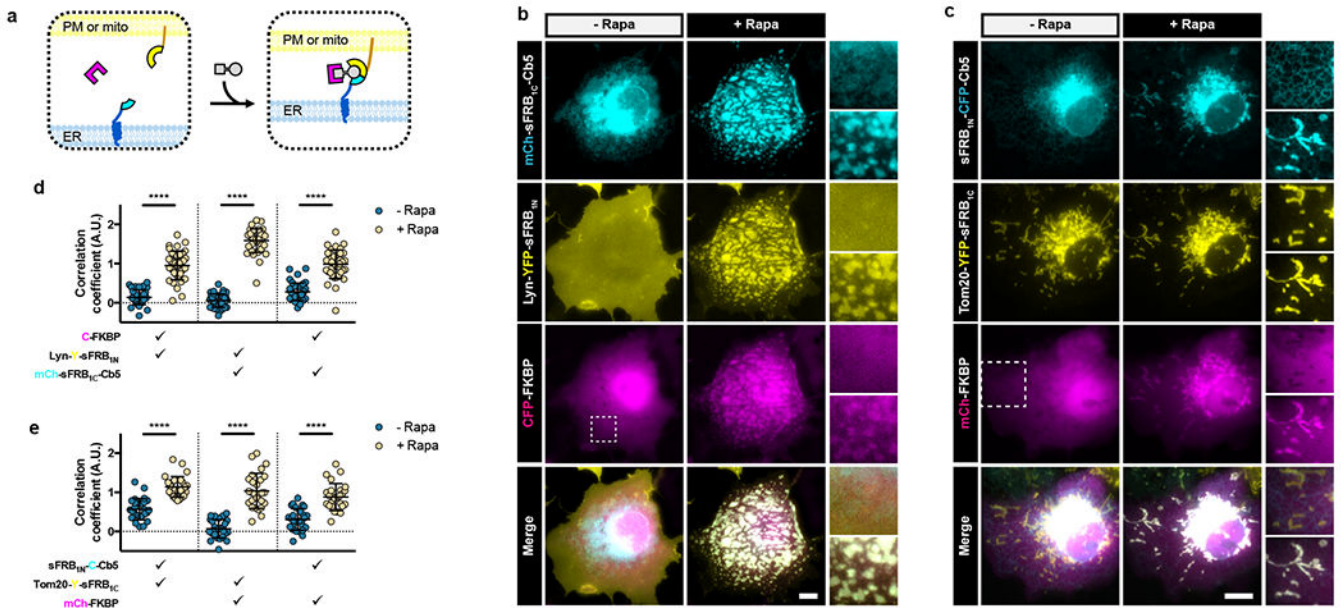


Figure 4: CIT-based recruitment of cytosolic protein to ER-PM and ER-mitochondria MCS.

(a) Targeting cytosolic FKBP (magenta) to ER-PM or ER-mitochondria MCS. sFRB halves (cyan and yellow) targeted to two organelles recruit FKBP in a rapamycin-dependent manner. (b) Cos-7 cells expressing mCh-sFRB_{1C}-Cb5, Lyn-Y-sFRB_{1N} and CF pre- and 12 min post-rapamycin for CF recruitment at ER-PM MCS. (c) Cos-7 cells expressing sFRB_{1N}-C-Cb5, Tom20-Y-sFRB_{1C}, and CF pre- and 12 min post-rapamycin for CF recruitment at ER-mitochondria MCS. (d, e) Trimerization quantification between the 3 signals pre- and post-rapamycin. Check marks specify each combination of two wavelengths used in calculating pairwise Fisher's transformation of Pearson's correlation coefficients. Data are presented as mean values \pm SD. Two-tailed Student's t-test assuming equal variance was used to compare correlations pre- and post- 100 nM rapamycin, p-values indicated in graph. (d) $n = 38$ cells, 3 independent experiments. (e) $n = 27$ cells, 3 independent experiments. Scale bars, 10 μ m.

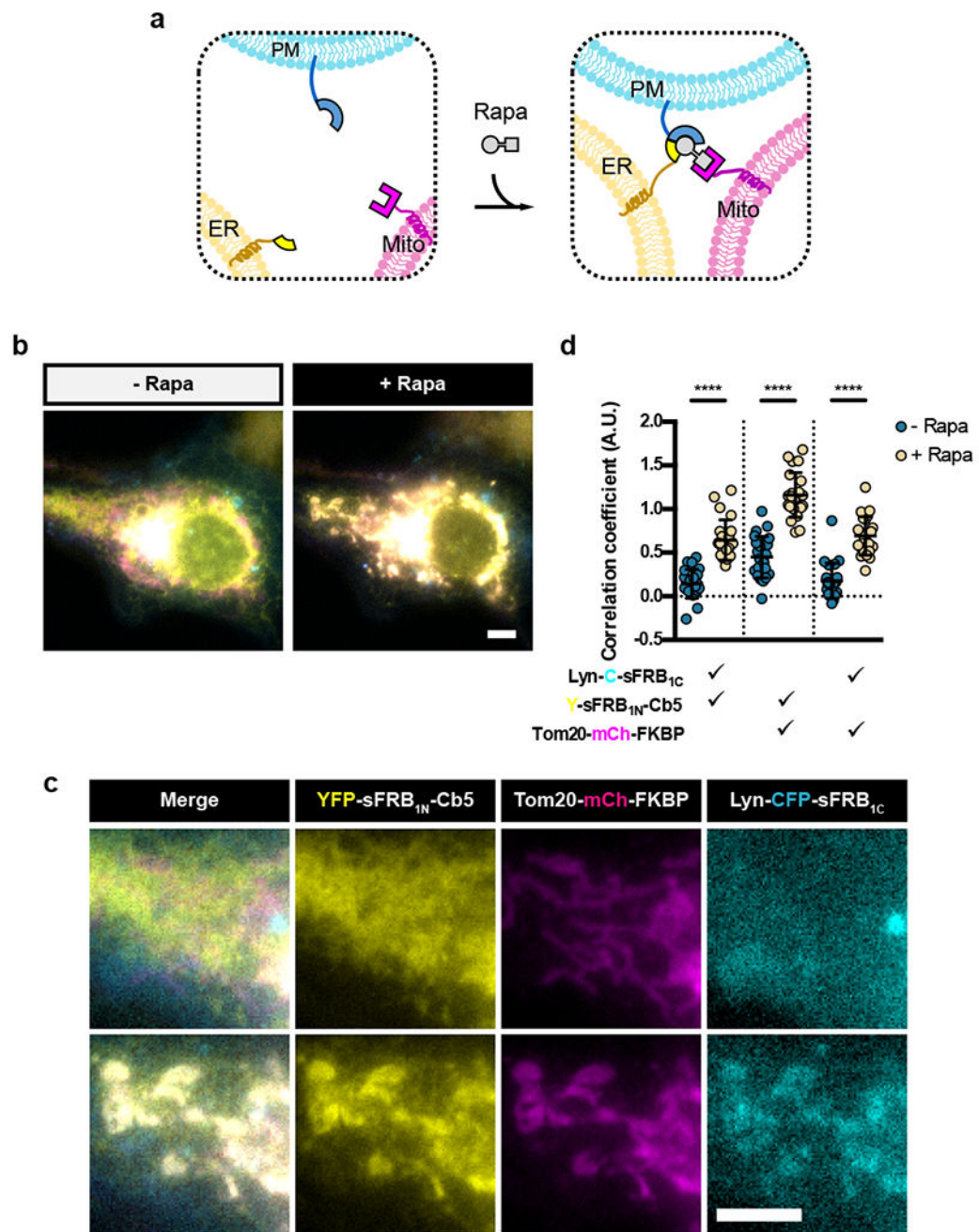


Figure 5: Tri-organelle junction formation by CIT.

(a) Trimerization of CIT components targeted to ER, mitochondria and PM by rapamycin. (b, c) Cos-7 cell expressing Y-sFRB_{1N}-Cb5, Tom20-mCh-FKBP and Lyn-C-sFRB_{1C} pre- and 15 mins post-rapamycin. (d) Quantification of trimerization extent through pairwise correlation of Fisher's transformation of Pearson's correlation coefficient between three wavelengths. Data are presented as mean values \pm SD. Two-tailed Student's t-test assuming equal variance was used to compare correlations pre- and post- 100 nM

rapamycin, p-values indicated in graph. $n = 23$ cells; 4 independent experiments. Scale bars, 5 μm .

Author Manuscript

Author Manuscript

Author Manuscript

Author Manuscript

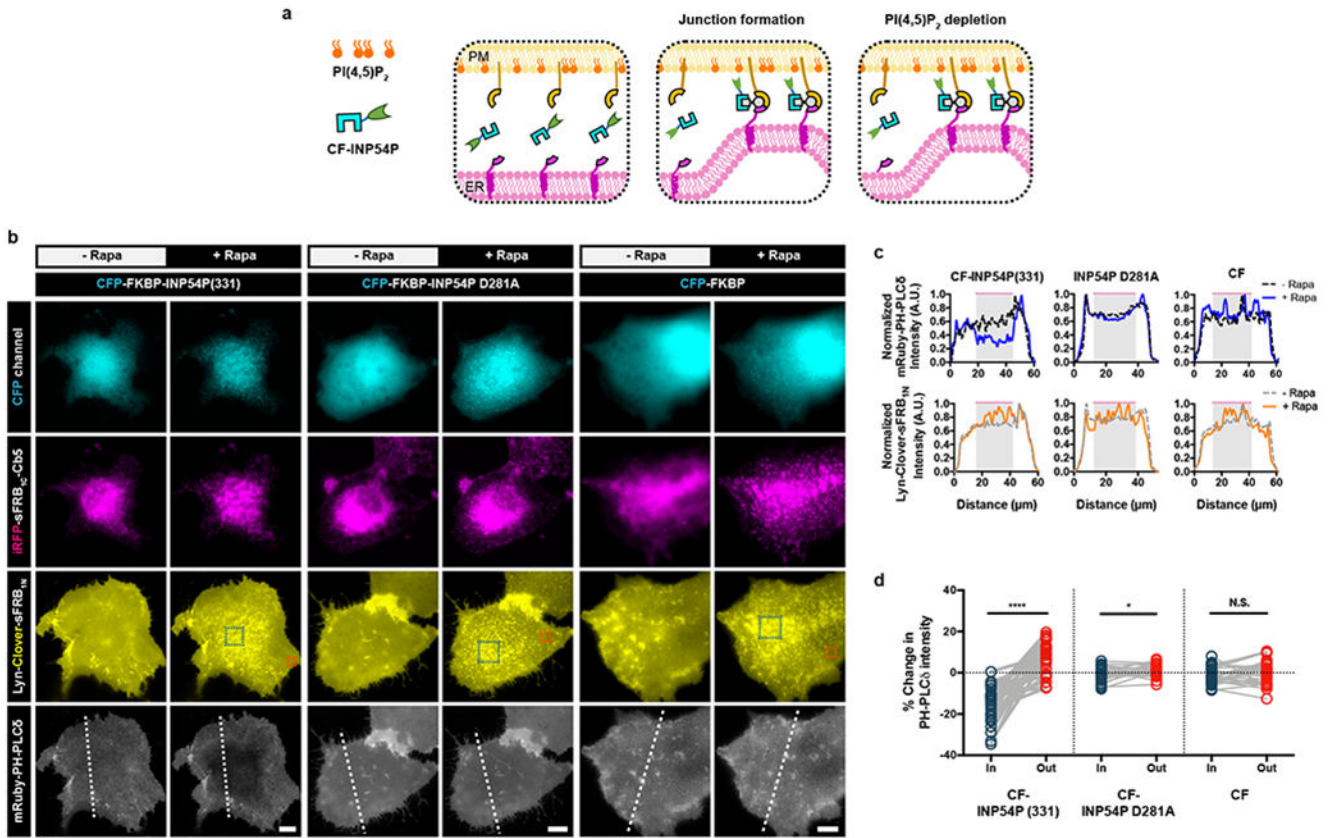


Figure 6: CIT induces local PI(4,5)P₂ depletion at ER-PM MCS.
 (a) Schematic of CIT-induced PI(4,5)P₂ depletion. CF-INP54P is recruited to ER-PM MCS by ER and PM localized sFRB halves. Upon junction formation (middle panel), INP54P accesses PM PI(4,5)P₂ leading to local PI(4,5)P₂ depletion (right panel). (b) Comparing effects of ER-PM MCS recruitment of functional CF-INP54P (331) against phosphatase-dead mutant CF-INP54P (D281A) and CF alone. Cos-7 cells also express Lyn-Clover-sFRB_{1N}, iRFP-sFRB_{1C}-Cb5 and mRuby PH-PLCδ, a PI(4,5)P₂ biosensor. Time-lapse epifluorescence microscopy taken pre- and 5 mins post- rapamycin addition. Teal and orange dotted boxes indicate regions inside and outside ER-PM MCS respectively. (c) Normalized intensity of mRuby PH-PLCδ PI(4,5)P₂ biosensor linescans from (b). Gray shaded regions with dotted magenta lines indicate high ER-PM junction formation. (d) Intensities of mRuby PH-PLCδ PI(4,5)P₂ biosensor of user-defined regions of interest inside and outside ER-PM MCS. Analyzed with two-tailed paired Students t-test assuming equal variance, p-values indicated in graph. Pairs from left to right: $n = 28, 25,$ and 23 cells; 4 independent experiments each. Scale bar, 10 μm.